Chapter

Transmission Electron Microscopy of Nanomaterials

Mohammad Jafari Eskandari, Reza Gostariani and Mohsen Asadi Asadabad

Abstract

Structural and analytical characterization, in the nanometer scale, has become very important for all types of materials in recent years. Transmission electron microscope (TEM) is a perfect instrument for this purpose, which is summarized in this chapter. Parameters such as particle size, grain size, lattice type, morphological information, crystallographic details, chemical composition, phase-type, and distribution can be obtained by transmission electron micrographs. Electron diffraction patterns of nanomaterials are also used to acquire quantitative information containing size, phase identification, orientation relationship and crystal defects in the lattice structure, etc. In this chapter, typical electron diffraction, high-resolution transmission and scanning transmission electron microscope imaging in materials research, especially in the study of nanoscience are presented.

Keywords: nanomaterials, characterization, transmission electron microscopy, electron diffraction

1. Introduction

Nanotechnology is considered to be the main technology for all types of materials in the current century. Nowadays, the development and production of nanostructure materials aimed at increasing the strength to weight of structures that led to cost and energy saving were considered by researchers [1, 2]. For studying materials in the nanometer scale, the investigation of nanostructures is needed to discover the properties of nanostructured materials. This purpose will not be achieved except by the use of efficient characterization instruments. Transmission electron microscope (TEM) has evolved over many years into a highly sophisticated instrument that has found widespread application across the scientific disciplines. Due to unparalleled ability to provide structural and chemical information over a range of length scales down to the level of atomic dimensions, TEM has developed into an indispensable tool for understanding the properties of nanostructured materials and in manipulating their behavior. The precise control of nanoparticles size, grain size, size distribution and homogeneity, lattice type, crystal structure, dispersion, chemical and physical property of phases such as number, morphology, and structure of the phases at the nano-level are characterized by TEM. Besides, this investigation attempts to demonstrate the effectiveness of EDP technique to the analysis of nanomaterial properties. Types of diffraction patterns such as ring, spot and Kikuchi patterns, and general and unique indexing diffraction patterns are described.

The methods for indexing simple, complicated and imperfect patterns as well as Kikuchi lines and a combination of Kikuchi lines and spots are determined.

In this research, samples of materials such as nanoparticles, nanotubes, bulk metallic, graphene, graphene oxide, and polymer nanocomposites are investigated using an EM208S (PHILIPS) transmission electron microscopy operating at an accelerating voltage of 100 kV and a digital camera. In addition, electron diffraction pattern of several materials are expounded and structure of materials is predicted with electron diffraction pattern results interpretation. On the other hand, TEM/STEM (STEM, JEOL JEM-2100F) equipped with an energy-dispersive X-ray spectrometry (EDS) and the operating voltage of 200 kV are used to evaluate the in-situ phase characterization, microstructural observation, dislocation pile-up and chemical composition of in-situ nanocomposite fabricated by planetary ball milling of Al/BN composite powders and hot extrusion. This paper discusses the basic principle and applications of the transmission electron microscope (TEM) in the field of nanotechnology research.

2. Transmission electron microscope

2.1 Preferred orientation and texture

In some samples, the preferred orientation of planes creates by several mechanical processes such as accumulative roll bonding (ARB), cyclic extrusion compression (CEC) and equal channel angular pressing (ECAP) processes, etc. TEM image and SAED pattern of nanostructured Al 2024 alloy under ECAP process were demonstrated in **Figure 1(a)** and **(b)**, respectively. The SAED pattern of preferred orientation and textured nanostructured materials was formed from many partial rings or incomplete rings. Diffraction pattern of such materials can be described as an intermediate sample between a single and polycrystalline material. The texture produced in materials can be studied by the interpretation of their SAED. The preferred orientation {110} [001] was formed in Al 2024 alloy by this process [3].

2.2 Dislocation

ECAP [3] and cryo-cross-rolling (CCR) process [4, 5] were carried out on Al 5083 and Al 1050 alloys, respectively. These two processes form a matrix with highly dislocation density, which changes the diffraction pattern. Besides, SAED patterns

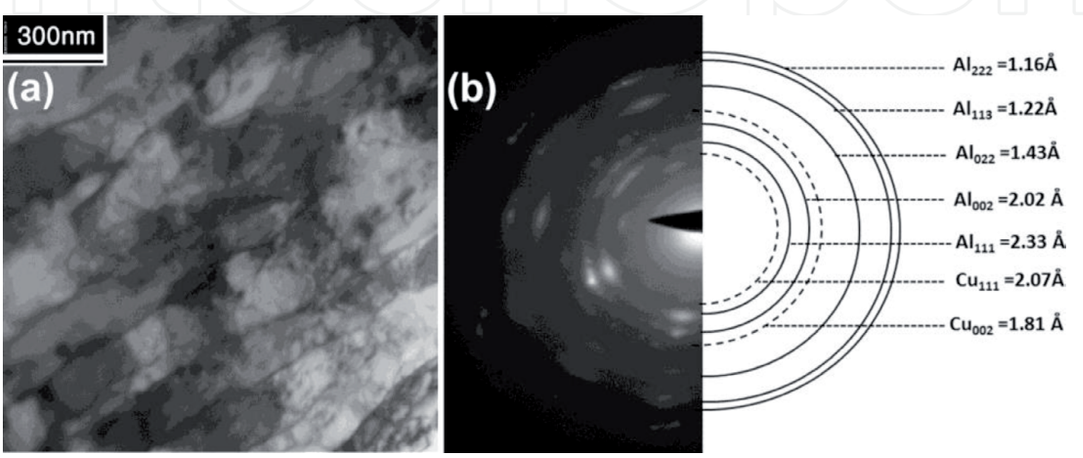

Figure 1.
(a) TEM image and (b) SAED of Al 2024 alloy under ECAP process [3].

of two alloys demonstrate streaks effects on spots pattern owing to highly pile-up of dislocations. Consequently, incomplete sectors of the rings in patterns were formed owing to preferred orientation in the crystal structure. Spots in the SAED pattern vary from a common shape to points with short and long tails. TEM images of nanostructured alloys and corresponding SAEDPs of the two samples demonstrated in **Figure 2**.

2.3 Kikuchi patterns

Kikuchi pattern consists of spots and paired parallel dark and bright lines. The spacing between a paired parallel dark and bright-line and the angle between Kikuchi lines in the pattern specify crystal structure characteristics such as the set of reflecting planes and distance of paired lines. By enhancing the thickness of the sample, the spots become more visible and the Kikuchi lines become less visible. Kikuchi patterns usually include spots and Kikuchi lines. Generally, Kikuchi patterns represent much more data rather than the spot patterns about crystal structure. The appearance of obvious Kikuchi pattern expresses a symptom of the ideal crystal. **Figure 3** displays the Kikuchi pattern of γFe with structural specifications [3].

Figure 4(a) illustrates TEM image of nanostructured Al 7075 alloy under thermomechanical processing. Tilting processing of the sample in TEM was applied to investigate the crystal lattice defects and orientation relationships. The SAED pattern includes the Kikuchi lines and spots of Al 7075 alloy was shown in **Figure 4(b)**.

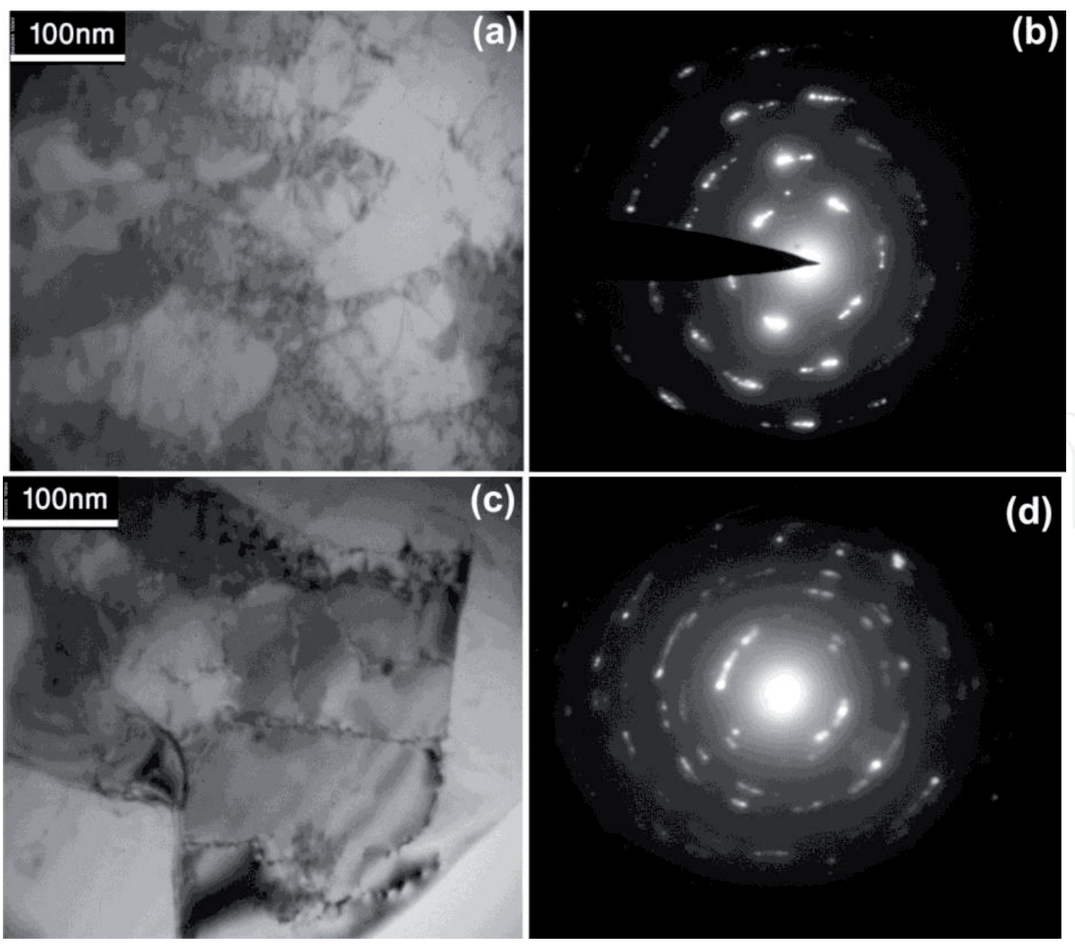

Figure 2.
(a) TEM images and (b) corresponding SAEDP of Al 5083 alloy under ECAP process [3], (c) TEM images and (d) corresponding SAEDP of Al 1050 alloy under CCR process [4, 5].

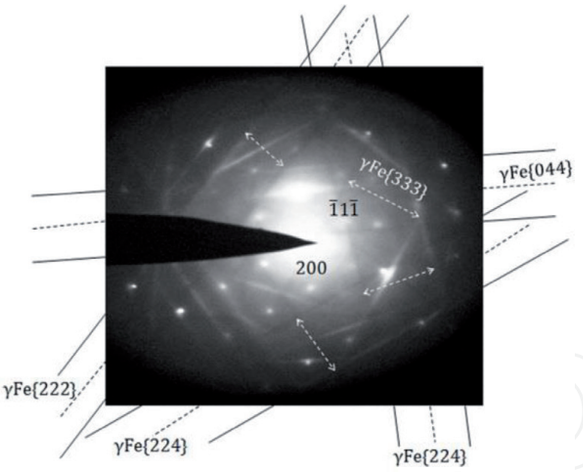

Figure 3.
Kikuchi pattern of γFe [3].

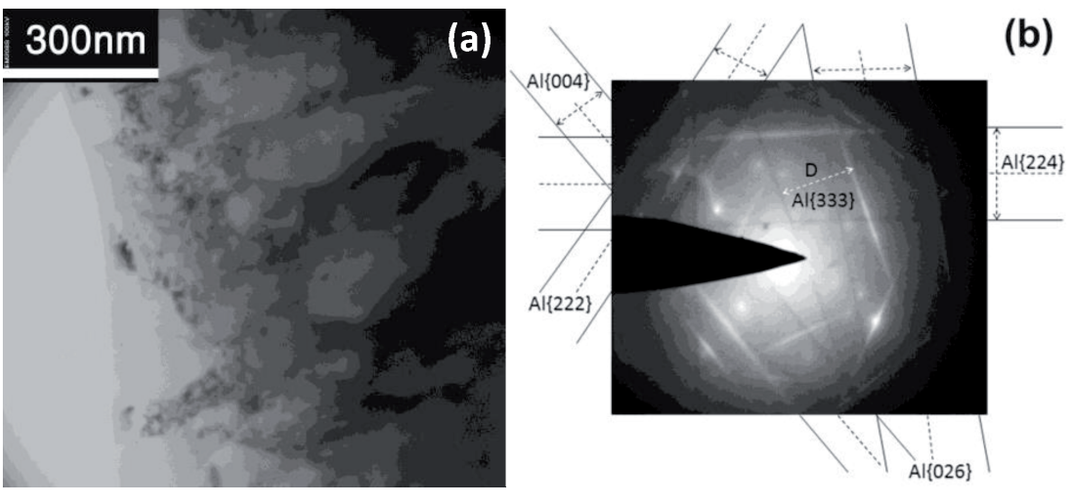

Figure 4.
(a) TEM image and (b) SAED pattern of nanostructured Al 7075 alloy [3].

The Kikuchi lines in SAED pattern were indexed the paired Kikuchi lines. Besides, crystal structure characteristics such as interplanar spacing and planes can be specified by measuring the distance between the paired Kikuchi lines [3].

2.4 Twinning

The twinning phenomenon has been known as the crystal structure defect and emerged principally as two parallel planes in TEM observations. In the twinning phenomenon, extra spots were produced surrounding the original spots of crystal structure in the pattern owing to the difference in orientation of twinning planes from the local crystal structure. TEM image and corresponding SAED pattern of twinning planes in *γFe* matrix with a f.c.c crystal lattice were indexed and shown in **Figure 5**, respectively. The main spots corresponding matrix pattern and twin spots with zone axis z = $[\bar{1}\,2\,3]$ were mirror reflections across the $(1\bar{1}\,1)$ [3, 6].

2.5 Core-shell nanoparticles

Investigation results of the fabrication of Au/Al_2O_3 core-shell nanoparticles were demonstrated by one-step, and a very fast method with continuous-wave fiber laser ablation on an Aluminum (Al) plate coated gold (Au) nanolayer film

immersed into ethanol. The core and shell of these nanoparticles contained complete crystalline structures. **Figure 6(a)** and **(b)** illustrates TEM images of Au/Al_2O_3 core-shell nanoparticles fabricated by the ablation of Al surface coated with Au a nanolayer. The shape of core-shell nanoparticles was approximately spherical and the single core-shell nanoparticle contains Au (core) and Al_2O_3 (shell), as shown in **Figure 6(b)**. The core and shell of the nanoparticles sometimes seemed entirely regular or non-regular. The core and shell of nanoparticles are determinable by the difference in contrast in TEM images. The structure of single core-shell nanoparticle includes completely crystalline gold (dark zone) coated by Al_2O_3 layer with crystalline structure (gray zone), as shown in **Figure 6(a)** and **(b)**. The Al_2O_3 shell of core-shell nanoparticle progressively has changed to the steady Al/Al_2O_3 compound by overtime. Phase characterization and crystalline planes of Au, Al, and Al_2O_3 were carried out by the use of the SAED technique, as shown in **Figure 6(c)** and **(d)** [7].

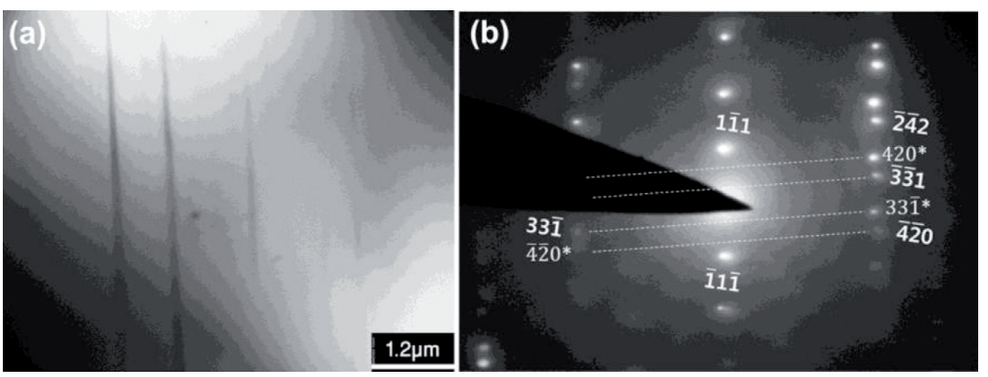

Figure 5.
(a) TEM image of twinning planes and corresponding SAED pattern of γFe *with f.c.c crystal lattice [3, 6].*

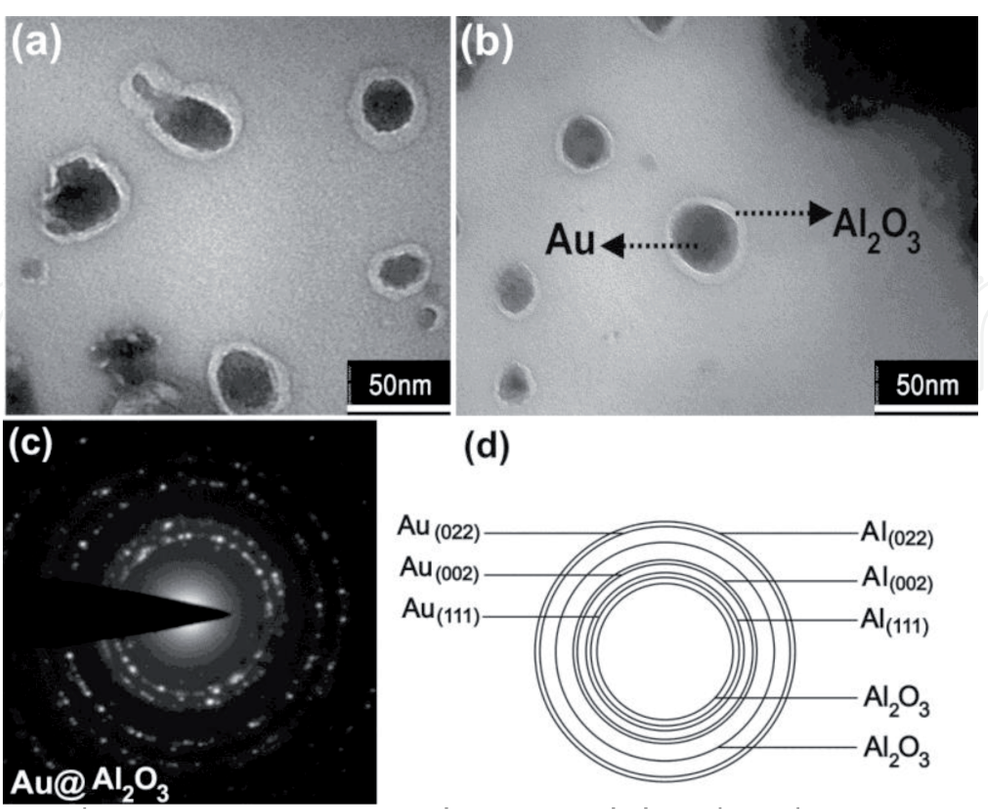

Figure 6.
(a, b) TEM images, (c) corresponding SAED and (d) analysis of ring pattern to identify phase and crystal planes of Au/Al_2O_3 core-shell nanoparticles [7].

By using of the EDP of individual nanoparticle, many of the crystalline structural properties can be measured such as interplanar spacing and the angles of the planes. TEM image of an individual Au/Al_2O_3 core-shell nanoparticle (**Figure 7(a)**) and the EDP of Au as a shell (**Figure 7(b)**) were demonstrated. In addition, the zone axis and planes of the shell were determined in accordance with standard patterns in **Figure 5(c)** and **(d)**. The spot and ring EDPs of core-shell nanoparticles corroborated of their crystalline specifications. By using of follow equation, lattice parameter of the shell was obtained.

$$\frac{1}{d^2} = \frac{h^2 + k^2 + l^2}{a^2} \quad (1)$$

where a is lattice parameter, d is interplanar spacing, and hkl are Miller indices. Lattice parameter of the core was calculated by using of Eq. (1) about a = 4.0502 Å which was near to the gold lattice parameter. Therefore, surely the core of these core-shell nanoparticles was gold [7].

2.6 Carbon nanotubes

Different types of carbon nanotubes (CNTs) have been one of the high potential materials for application in nanotechnology. In this work, the basic features of multiwall carbon nanotubes (MWCNTs) direct production on metal catalyst particles via thermal chemical vapor deposition (T.CVD) with existence of zirconium hydride (ZrH_2) and Al nanoparticles were investigated. **Figure 8(a)** and **(b)** illustrate TEM image of MWCNTs that the catalyst nanoparticles are various parts of nanotubes. The average size of the catalyst nanoparticles was about 20 nm. Thus, the considerable effect of ZrH_2 particles on the decreasing of the metal particles was clearly specified. Moreover, **Figure 8(c)** and **(d)** indicate the physical properties of MWCNTs such as the well-graphitized walls and open caps of them, respectively [8].

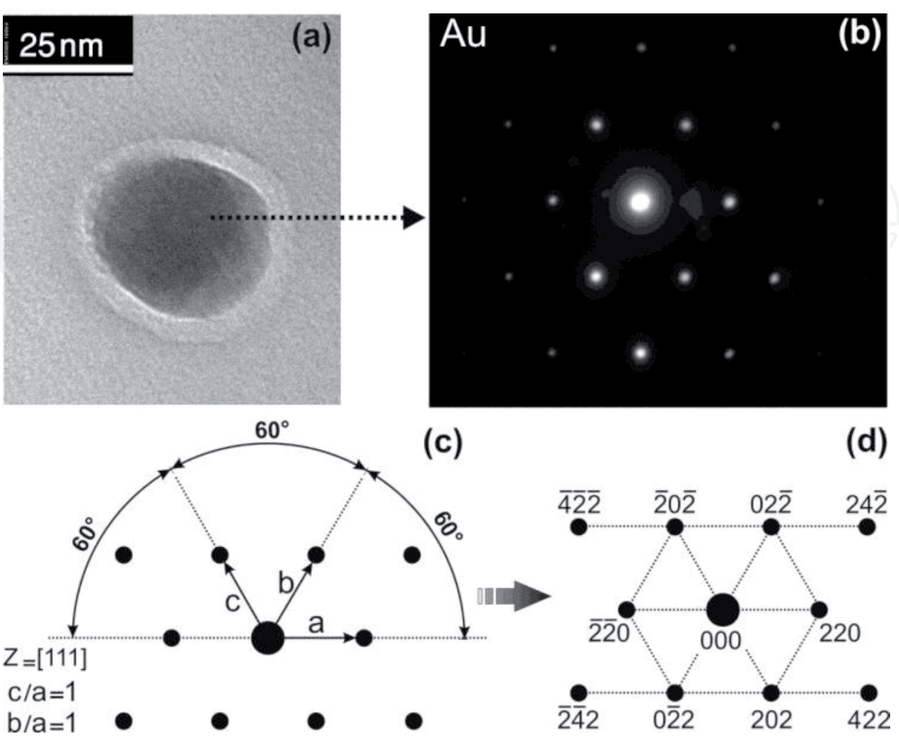

Figure 7.
(a) TEM image of Au/Al_2O_3 core-shell nanoparticles, (b) corresponding SAED of single nanoparticle core, (c, d) analysis of spot pattern to determined phase and crystal planes [7].

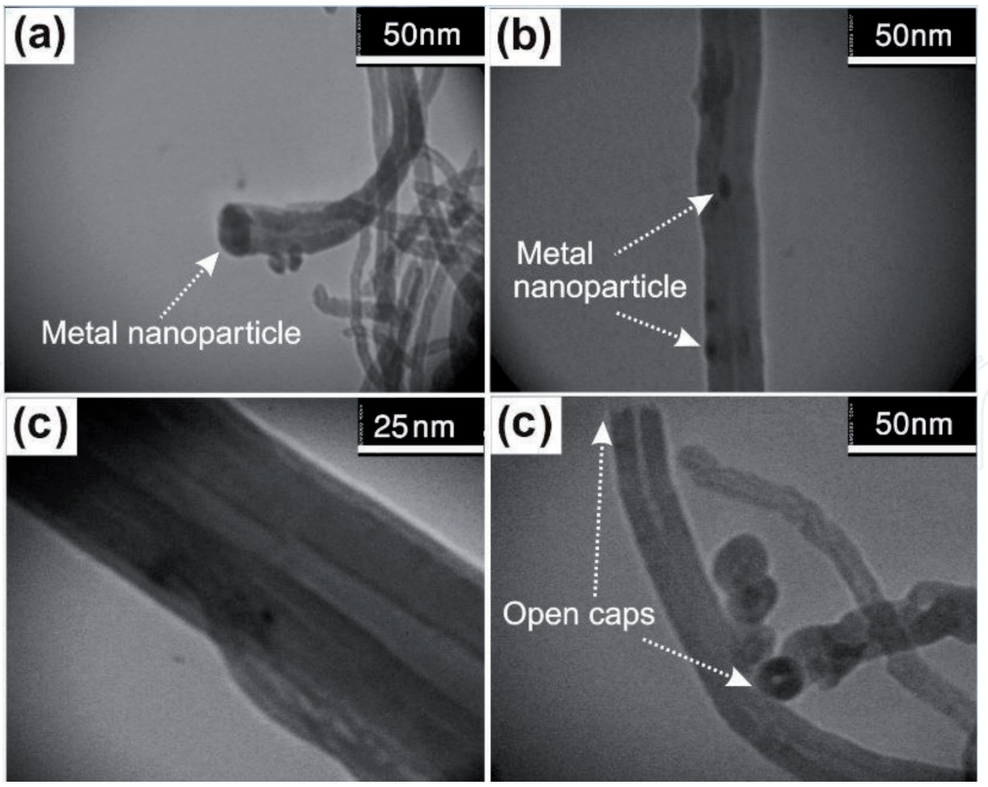

Figure 8.
TEM images of MWCNTs (a), (b) with catalyst nanoparticles, (c) and (d) with physical properties [8].

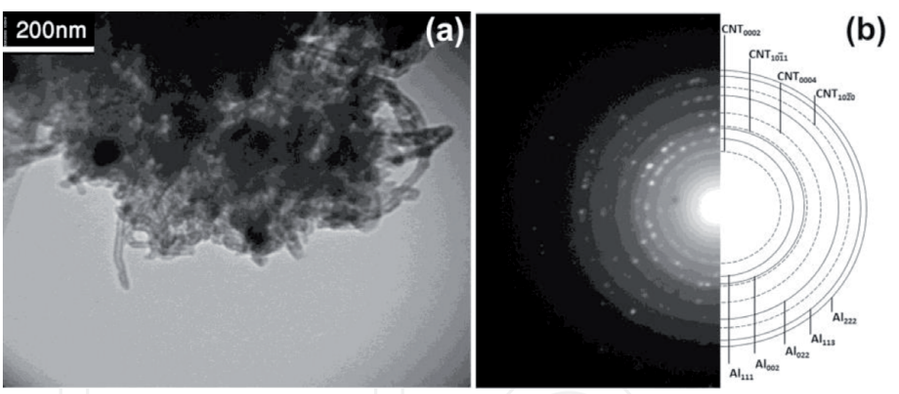

Figure 9.
(a) TEM image and (b) the SAED pattern of MWCNT/Al composite [9].

Compound of carbon nanotubes (CNTs) and metal nanoparticles has displayed considerable features. The major problem in CNTs-reinforced compound has been the regular dispersion of CNTs in nanoparticles. Ball milling technique as an effective method has been progressed for dispersion of the CNTs in micro and nanoparticles. For instance, 20 wt. % MWCNT+Al microparticle was compounded by ball milling method and studied using TEM and EDP technique as well. **Figure 9(a)** and **(b)** demonstrate TEM image and corresponding EDP of MWCNT/Al nanoparticles composite, respectively. Type of phases and crystal planes of MWCNTs and Al nanoparticles were identified, as shown in **Figure 9(b)** [9].

3. Transmission electron microscopy in the study of Al/BN Nanocomposite

The fabrication of bulk Al-BN nanocomposites have strongly been considered due to several advantages such as their light weight, superior mechanical properties

even at low contents of BN as a reinforcement, and good thermal stability at elevated temperatures. These advantages are definitely related to the special characteristic of BN. It is well recognized that BN decomposed and dissolved in the Al matrix during high energy ball milling. Then, the possible AlN and AlB_2 as the in-situ phases are generated during a heating state in the Al matrix [10–17]. Due to presence of in-situ particles in matrix, the microstructural observation and mechanical behavior of the in-situ Al/BN nanocomposite should be investigated by high resolution transmission electron microscopy.

3.1 Phase evaluation

In the recent study, Al-1,2 and 4 wt. % BN bulk nanocomposite was fabricated by planetary ball milling of the composite powders and a post-process of hot extrusion at 580°C. As can be seen in **Figure 10**, the rod-shape phase was detected in TEM observation. Although AlN and AlB_2 as the in-situ phases were expected to create in microstructure, the accurate investigation using STEM has shown different results. As can be seen in **Figure 11**, the nature of the rod-shape phase was recognized by high-resolution STEM micrographs. The plane of atoms is clearly visible in the micrograph. The inter-planar spacing as the finger effect can lead to phase characterization. This parameter for the rod-shaped phases is measured to be about 0.55 nm, which is corresponding to the (006) planes of unwanted in-situ Al_4C_3 phase, respectively.

Figure 12 shows the bright-field TEM image of Al_4C_3 phase with the corresponding result of the EDS line scan the matrix and in-situ phase in the Al-2 wt. % BN nanocomposite. As can be, the high amount of carbon in analysis confirms the presence of Al_4C_3. In addition, the decreasing blue line and increasing the gray line in scanning through the in-situ phase corresponded to the contents of Al and carbon elements, respectively which were proved the formation of Al_4C_3.

The EDS analysis as a valuable technique in TEM is used to characterize Al_4C_3 in-situ phases in the microstructure of the Al-2 wt. % BN nanocomposite (**Figure 13**). Although the EDS technique does not accurately determine the composition, the results show the increasing the carbon content in the in-situ phase against the matrix in composition. Stearic acid as the process control agent (PCA) was recognized as the source of carbon in the nanocomposite. In fact, the PCA dissolved in the matrix during the planetary ball milling and Al_4C_3 was formed after hot extrusion as following reaction [18]:

$$4Al + 3C = Al_4C_3 \quad (2)$$

The SAED pattern of nanocomposite was shown in **Figure 14**. The continuous ring shape in the SAED pattern confirms that the nano crystallite structure was developed in the nanocomposite. In addition, the Al_4C_3 (012) and Al_4C_3 (0015) rings were observed in this pattern. Although the characterization of phases with the light elements such as nitrogen is troublous, the presence of AlN phase was shown in **Figure 14**. The diffraction reflections of AlN (100) in the SAED pattern indicate its in-situ formation through the extrusion process by the following equation:

$$Al + N = AlN \quad (3)$$

AlN phase as spherical shape and nanometric size was found in microstructure observation using STEM and the EDS analysis (**Figure 15**). As can be seen, increasing the nitrogen content compared to the matrix confirms the creation of

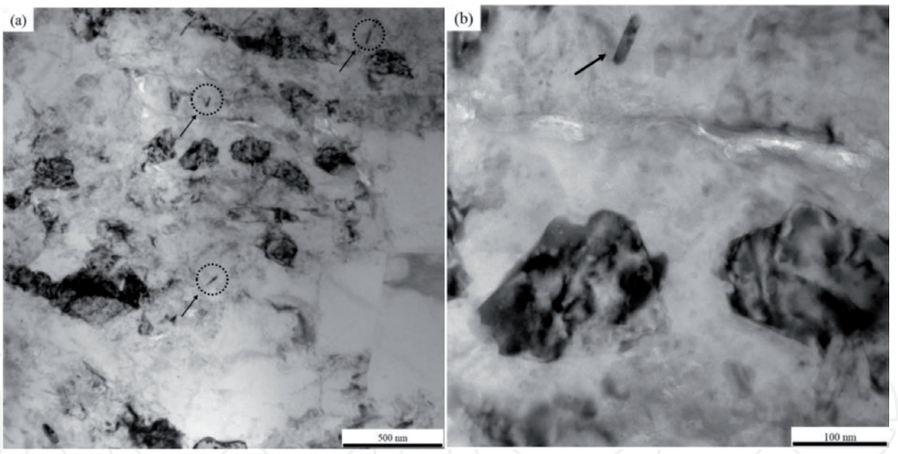

Figure 10.
TEM micrograph of Al-1 wt. % BN representing (a) the uniform distribution of a rod-shape in-situ phase and (b) higher magnification.

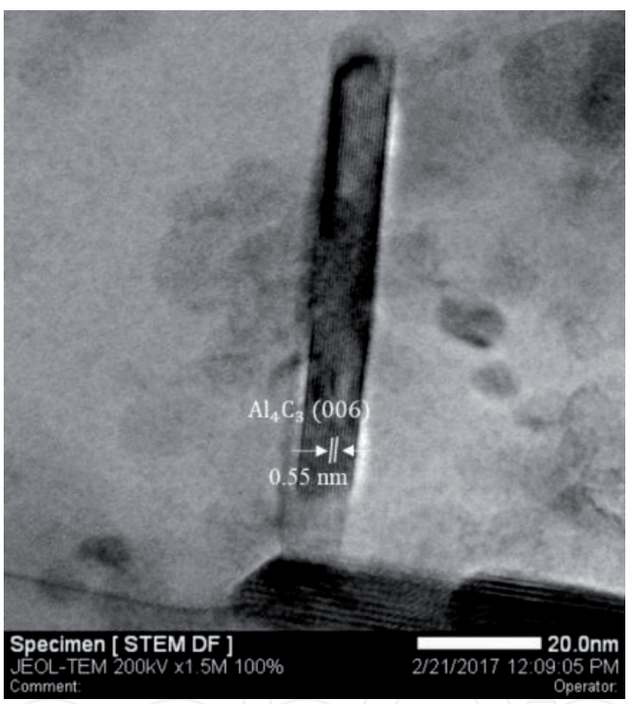

Figure 11.
High resolution STEM image of the in-situ Al_4C_3 phase with orientation of (006).

AlN in the matrix. Furthermore, the green line in the result of the EDS line scanning shows the higher nitrogen content of the spherical shape phase. According to the composition table in point (1), the high fraction of Nitrogen and all the Boron content remained as a solid solution in the matrix. These elements appeared as a solid solution during high energy ball milling in the Al matrix. Therefore, AlN phase was created with the reaction of Al and N in the hot extrusion process. On the other hand, AlB_2 which can be formed from the reaction of Al and B was not found.

Figure 16 shows the fraction of Al_2O_3 phase in the microstructure. As can be seen, the high content of oxygen compared to the matrix is clearly observed as a yellow line in the result of line scanning and the EDS analysis. Therefore, due to the limitation of XRD to detect the in-situ phase which has less than 5 vol. % in the matrix, the phase evaluation of this nanocomposite with the nano- and low content of phases is impossible using XRD.

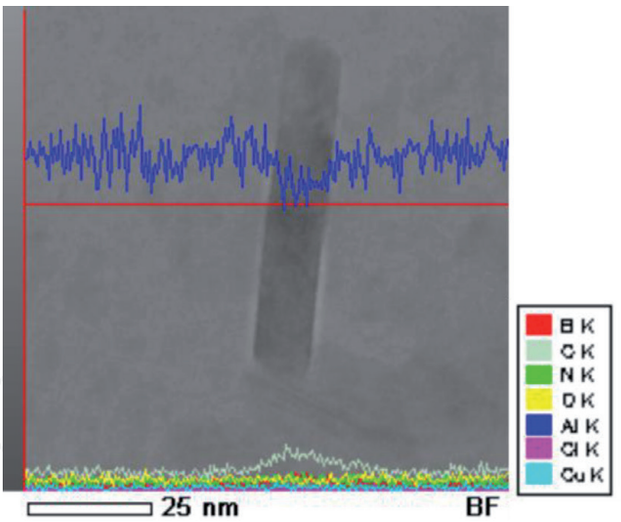

Figure 12.
Bright field TEM image of Al4C3 phase with the corresponding result of the EDS line scan.

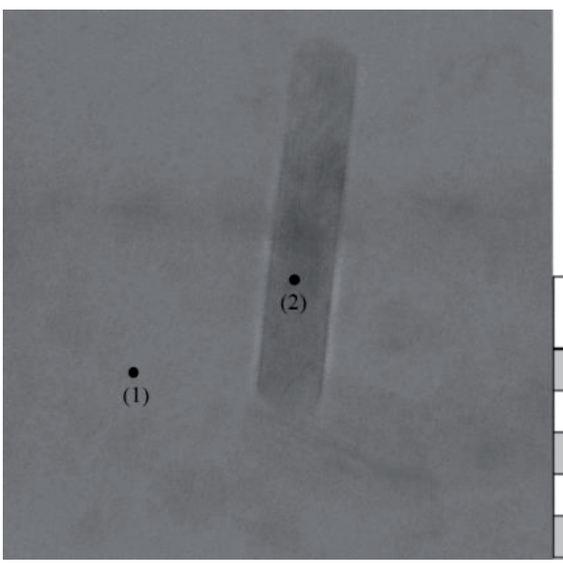

Elements	Atomic Percent (point 1)	Atomic Percent (point 2)
Al	77.07	48.77
C	14.73	43.4
N	5.95	5.88
O	2.25	1.95
B	-	-

Figure 13.
Bright field TEM images and the corresponding results of EDS analysis of the matrix and in-situ Al4C3 phases in Al-4 wt. % BN nanocomposite.

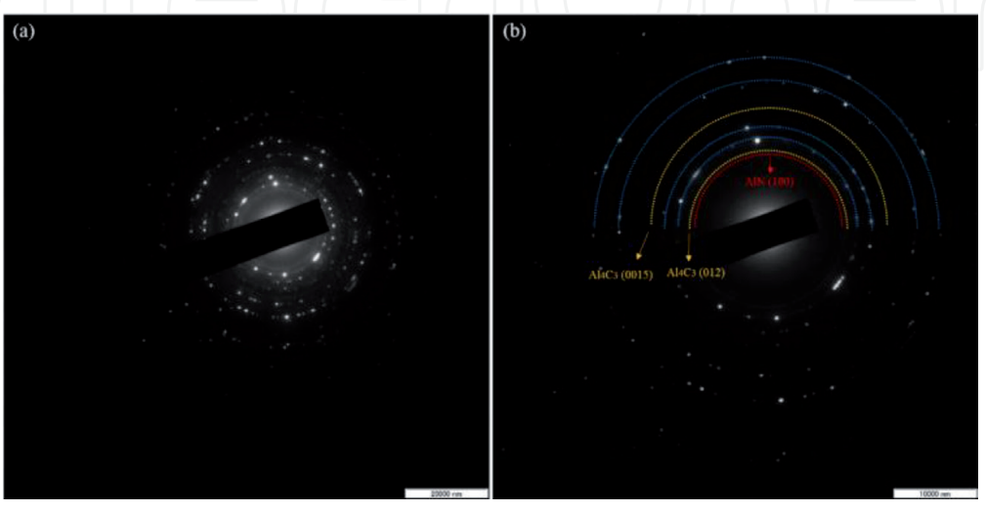

Figure 14.
(a) SAD pattern of Al-4 wt. % BN nanocomposite (b) higher magnification of SAD pattern of Al phase (blue color), the in-situ Al4C3 (yellow color) and AlN (red color) phases.

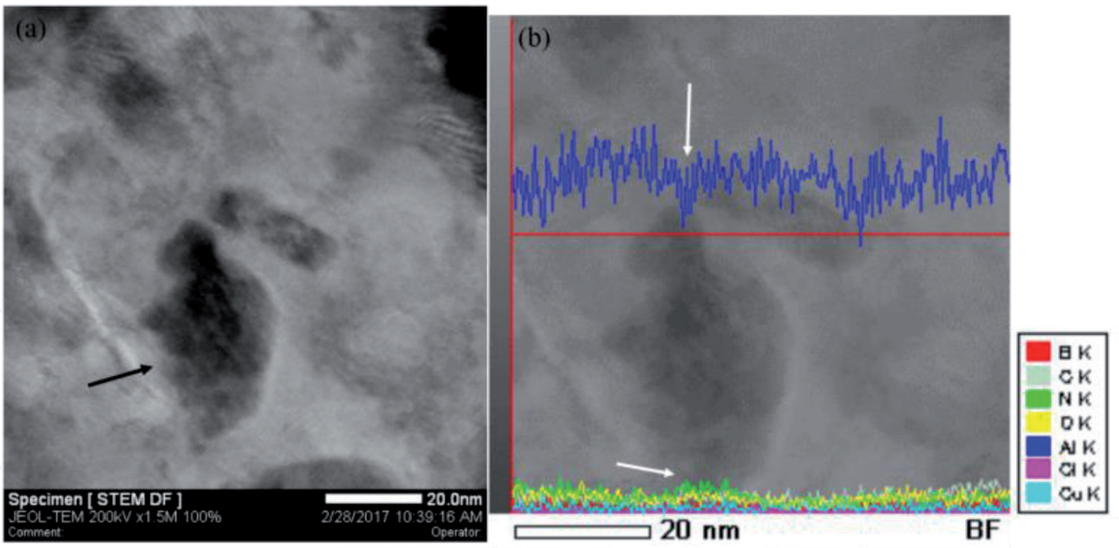

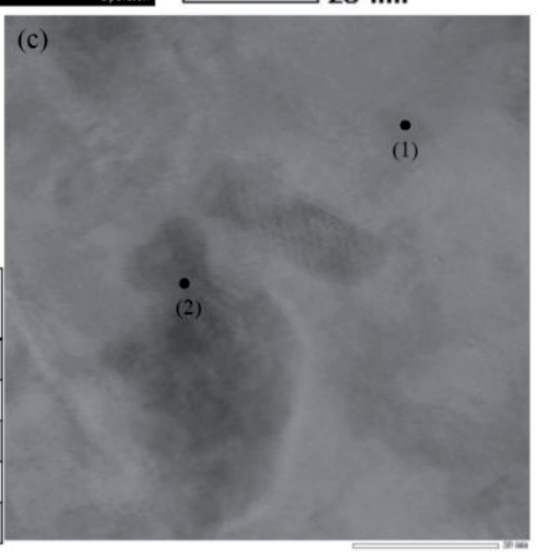

Elements	Atomic Percent (point 1)	Atomic Percent (point 2)
Al	83.72	83.19
N	8.23	11
B	1.52	-
O	3.36	2.76
Cu	3.17	3.05

Figure 15.
In-situ AlN phases in Al-4 wt. % BN nanocomposite (a) high resolution STEM image, (b) the EDS line scanning analysis, and (c) composition of the Al matrix and AlN phases.

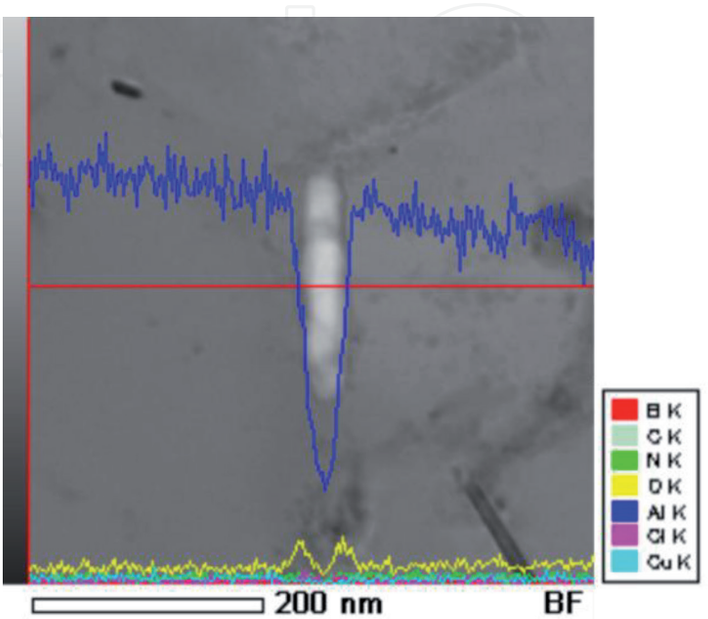

Figure 16.
The EDS line scanning analysis of Al_2O_3 phases in Al-1 wt. % BN nanocomposite.

3.2 Dislocation

Dislocation recognized as a linear defect is the justifier deformation mechanism. Density dislocation is a key factor is Calculated or estimated with a different method. Absolutely, the measuring corresponding to the observation of dislocations has more accurate than estimation with equations. In the mentioned nanocomposite, the TEM observation in **Figure 17** shows the cell wall dislocation and pile-up dislocation behind the grain boundary. As can be seen, the grain boundary in grain 1 acts as an obstacle against the dislocation movement. It led to pile up dislocation and stored strain in grain 1, while relaxation happened in the other adjacent grains with low dislocation density.

According to the following equation and TEM observations, the density dislocation (ρ) is calculated as a function of average separation between dislocations ($\bar{l}$) [19].

$$\bar{l} = 1/\rho \wedge 0.5 \tag{4}$$

Based on TEM observations and mentioned above equation, the dislocation density in the cell walls, accumulated behind the grain boundaries and in the grain interior are measured as 1.8×10^{16} m^{-2}, 7×10^{14} m^{-2}, and 1.5×10^{14} m^{-2}, respectively.

Figure 18 shows the incidence of extended dislocation was intersected on two slip planes. In this phenomenon, the new partial dislocation was created by intersecting of two leading partial dislocation, which is known as a stair-rod dislocation. In this dislocation, three dislocations were connected by wedge shape stacking fault and were immobile which is named Lomer-Cottrell lock. This is a barrier that pins the dislocation and led to work hardening in FCC materials [20].

Orowan dislocation loops in **Figure 19** indicate that dispersed phases such as Aluminum oxide particles in this nanocomposite act as the obstacle in dislocation movement.

3.3 Microstructural observations

Figure 20 displays the microstructure of nanocomposite after the hot extrusion process. As can be seen, the low angle boundary with the thick wall with an average thickness of 20 nm is surrounded by high angle boundaries. The cell

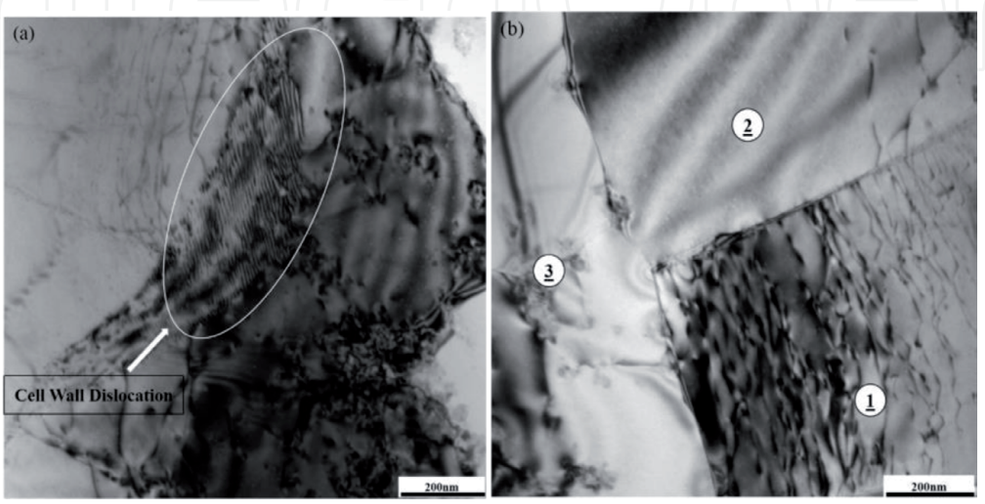

Figure 17.
TEM observation of dislocation in Al-4 wt. % BN nanocomposite (a) dislocation in cell wall and pile up dislocations behind the cell wall (b) accumulated dislocation near a grain boundary.

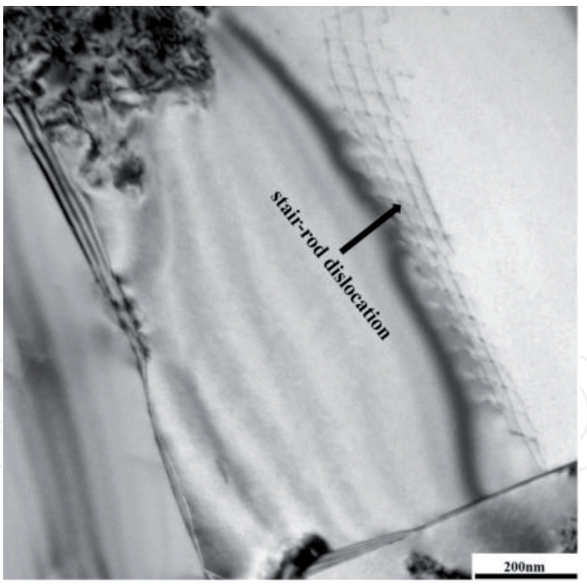

Figure 18.
Image of in Al-4 wt. % BN nanocomposite.

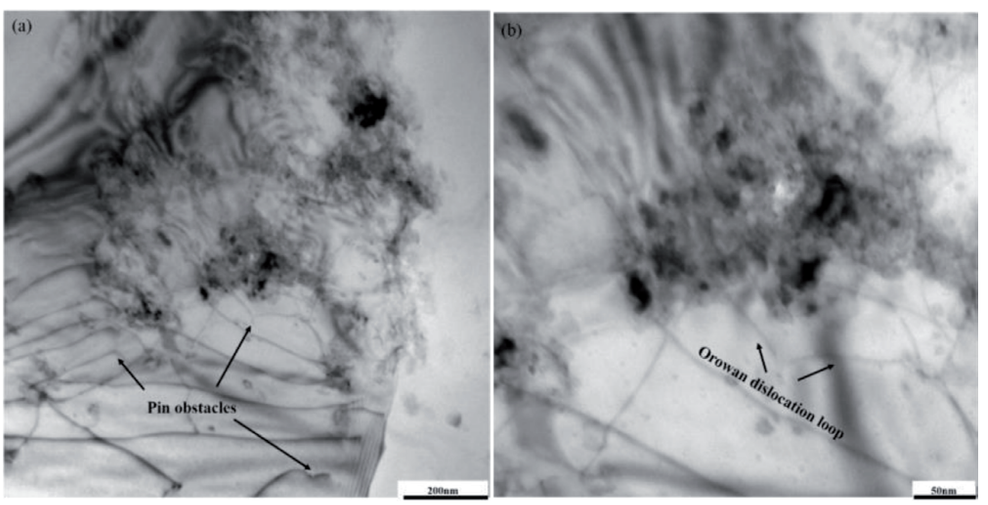

Figure 19.
Orowan dislocation loop (a) pin obstacles (b) higher magnification of Orowan dislocation loop.

structure happens in hot deformation of high SFE materials with converting three-dimensional dislocation tangles to two-dimensional dislocations with the more than 10° crystallographic misorientation. Then, the dislocation substructure is obtained from cell structure when the misorientation of cells exceeds to 2°. The dislocation substructures are converted to high angle sub boundaries which are surrounded by high angle boundaries [20].

Figure 21 shows the microstructure of Al-1 wt. % BN nanocomposite from the extrusion direction and cross-section of the extruded rod. As can be seen, the matrix consists of recrystallized nano/ultrafine grains with high angle boundaries and free dislocation density. It means the in-situ nanocomposite has thermal stability against the abnormal grain at high extrusion temperature.

Based on TEM observations and the high true strain value in hot extrusion process (2.3 mm/mm) which is higher than required critical strain for happening dynamic recrystallization in Al matrix (0.5 mm/mm), the recrystallization is the dominant mechanism in hot extrusion and high fraction of boundaries are formed as the high angle in microstructure [21]. On the other hand, the low angle boundaries and the grains with the high dislocation density were observed in microstructure

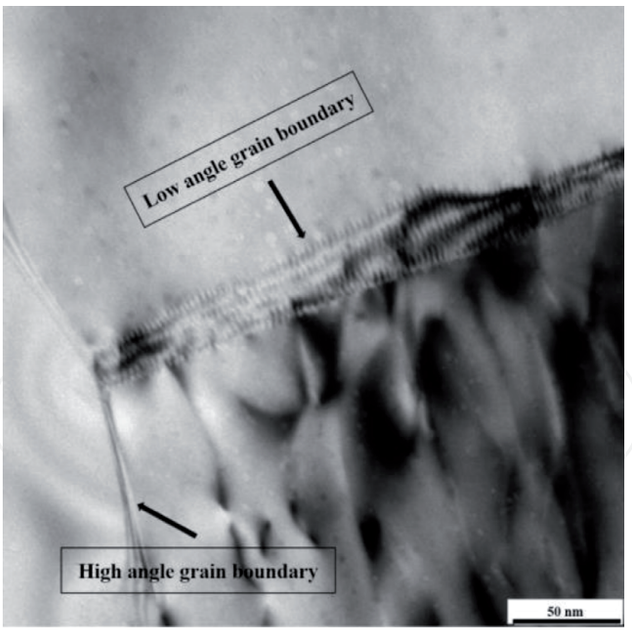

Figure 20.
Image of low angle grain boundary surrounded by high angle grain boundaries (Higher magnification views from ***Figure 19(b)****).*

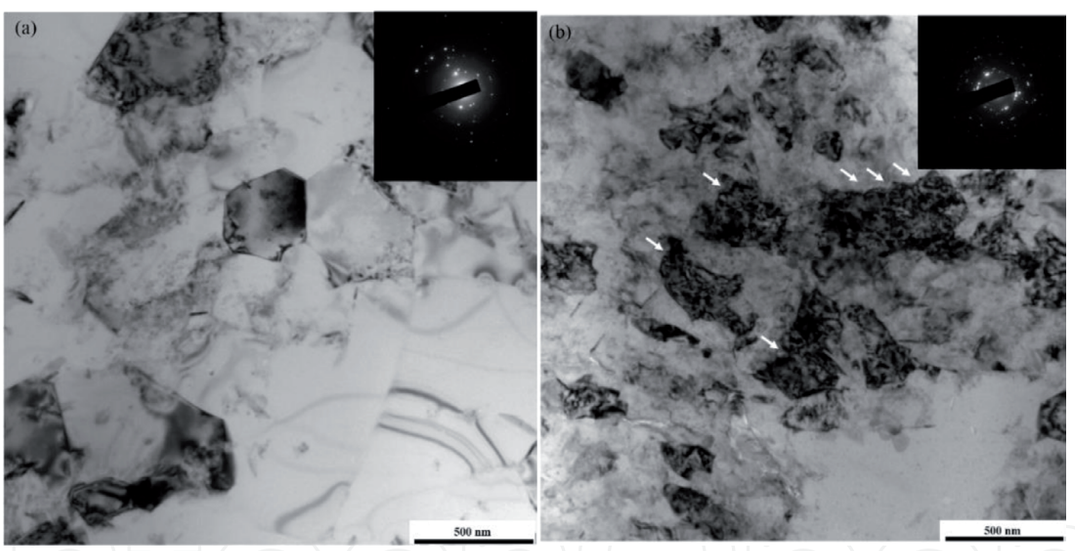

Figure 21.
Microstructure of Al-1 wt. % BN nanocomposite from (a) cross section of extruded rod (b) extrusion direction. Arrows show the scalloped boundaries.

(**Figure 22**). As can be seen, it seems that the rotation and coalescence is the main mechanism to decrease the low angle boundary. Due to high extrusion temperature, high stacking fault energy of Al matrix and high straining, the dynamic recovery occurred in the initial stage of deformation and the dislocations rearrangement themselves as low angle boundaries and subgrains is formed.

The geometrically necessary dislocation in metal matrix composite is high and led to increase in the kinetics of recrystallization [22–24]. However, the identification of dynamic recrystallization mechanisms in materials is difficult. The continuous dynamic recrystallization (CDRX) and the geometrical dynamic recrystallization (GDRX) can also occur simultaneously. During deformation of high stacking fault energy materials in elevated temperature, dynamic recovery prevents the accumulation of dislocation and the occurrence of discontinuous dynamic recrystallization (DDRX) will sustain. In CDRX, the subgrains are developed and

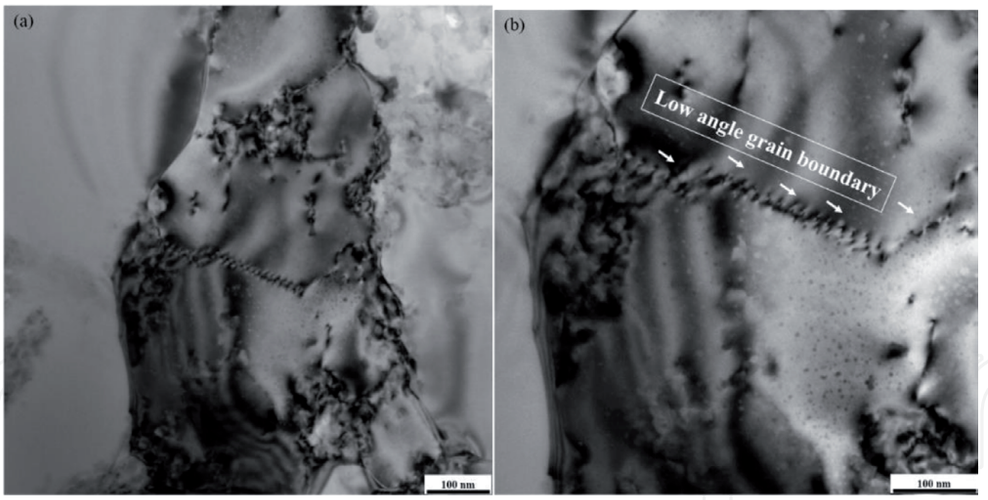

Figure 22.
(a) Microstructure of Al-4 wt. % BN nanocomposite from and (b) higher magnification.

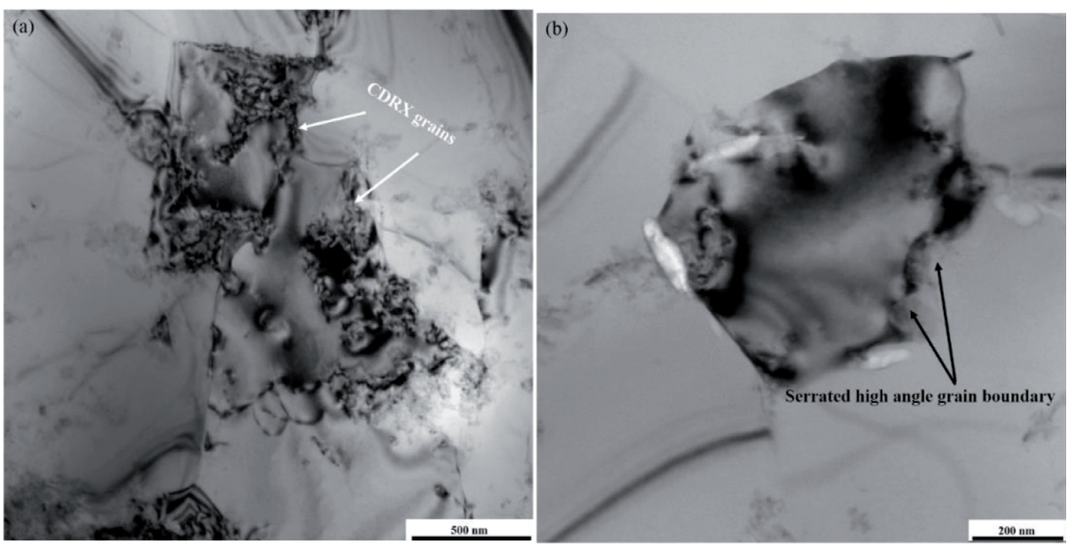

Figure 23.
Bright field TEM images of recrystallized grains in Al-4 wt. % BN (a) CDRX grains (b) GDRX grains.

then with increasing the misorientation of subgrain boundaries, the high angle grain boundaries will appear. On the other hand, in pure, solute drag and particle-containing alloy systems with high stacking fault energy which are deformed to large strain at high temperature, the GDRX will take place. In GDRX, the serrations are developed on the high angle boundaries and the scalloped boundaries are formed. In large straining, the grain elongation and thinning occurred. Then, the impingement of serrated boundaries led to equiaxed grains formation [22–26]. **Figure 23(a)** shows the ultrafine grains were recrystallized by CDRX. As can be seen in **Figures 21** and **23(b)**, the serrated high angle boundaries were observed. According to TEM results, the CDRX and GDRX are recognized as the dominant mechanisms in high angle grain boundary formation.

4. Conclusions

In summary, TEM/STEM with an energy-dispersive X-ray spectrometry corresponding to selected area diffraction patterns (SADP) is a powerful and accurate instrument to analysis and results from interpretation of nanomaterial lattice

structure. By using its technique, most of the nanomaterial structural properties can be characterized such as orientation relationship determination, phase identification, twinning, second phases, crystallographic information, dislocation, preferred orientation and texture, extra spots and streaks. In addition, steps of structural changes (lattice parameter and interplanar spacing) and reducing of nanoparticles and nano-grains sizes of different materials can be investigated by taking the EDPs of nanoparticles synthesis or nanostructuring process steps.

Acknowledgements

The authors would like to thank the TEM laboratory in Advanced Materials Group of Materials Research School for their financial supports.

Author details

Mohammad Jafari Eskandari[1*], Reza Gostariani[2] and Mohsen Asadi Asadabad[2]

1 Department of Materials Engineering, Isfahan University of Technology, Isfahan, Iran

2 Nuclear Science and Technology Research Institute, Iran

*Address all correspondence to: m_jafari@ma.iut.ac.ir

References

[1] Sabirov I, Enikeev NA, Murashkin MY, Valiev RZ. Bulk Nanostructured Materials with Multifunctional Properties. Cham/Heidelberg/New York: Springer; 2015

[2] Murty BS, Shankar P, Raj B, Rath BB. Textbook of and Nanoscience Nanotechnology. India: Universities Press; 2013

[3] Asadi Asadabad M, Jafari Eskandari M. In: Janecek M, Kral R, editors. Electron Diffraction, Modern Electron Microscopy in Physical and Life Sciences. Rijeka: InTech; 2016. pp. 2-26

[4] Jafari Eskandari M, Asadi Asadabad M, Tafrishi R, Shafyei A. Evolution of nanostructure in Al 1050 sheet deformed by cryo-cross-rolling. JMEPEG. 2016;**25**:1643-1649

[5] Jafari Eskandari M, Asadi Asadabad M, Tafrishi R, Bagherzadeh M. The effect of cross-rolling process on nanostructure of Al 1050 alloy. Journal of Nanoanalysis. 2014;**1**(2):93-98

[6] Asadi AM, Jafari EM. Transmission electron microscopy as best technique for characterization in nanotechnology. Synthesis and Reactivity in Inorganic, Metal-Organic, and Nano-Metal Chemistry. 2015;**45**:323-326

[7] Jafari Eskandari M, Shafyei A, Karimzadeh F. One-step fabrication of $Au@Al_2O_3$ core-shell nanoparticles by continuous-wave fiber laser ablation of thin gold layer on aluminum surface: Structural and optical properties. Optics and Laser Technology. 2020; **126**:106066

[8] Hasanzadeh I, Jafari Eskandari M. Direct growth of multiwall carbon nanotube on metal catalyst by chemical vapor deposition: In situ nucleation. Surface and Coating Technology. 2020;**381**:125109

[9] Jafari Eskandari M, Asadi Asadabad M, Tafrishi R, Emamalizadeh M. Transmission electron microscopy characterization of diffraction nanotubes. Inorganic and Nano-Metal Chemistry. 2017;**47**(2):197-201

[10] Xia Z, Li Z, Lu C, Zhang B, Zhou Y. Structural evolution of Al/BN mixture during mechanical alloying. Journal of Alloys and Compounds. 2005;**399**:139-143

[11] Firestein KL, Steinman AE, Golovin IS, Cifre J, Obraztsova EA, Matveev AT, et al. Fabrication, characterization and mechanical properties of spark plasma sintered Al–BN nanoparticle composites. Materials Science and Engineering A. 2015;**642**:104-112

[12] Firestein K, Corthay S, Steinman A, Matveev A, Kovalskii A, Sukhorukova I, et al. High-strength aluminum-based composites reinforced with BN, AlB2 and AlN particles fabricated via reactive spark plasma sintering of Al-BN powder mixtures. Materials Science and Engineering A. 2017;**681**:1-9

[13] Gostariani R, Ebrahimi R, Asadi Asadabad M, Paydar MH. Mechanical properties of Al/BN nanocomposites fabricated by planetary ball milling and conventional hot extrusion. Acta Metallurgica Sinica (English Letters). 2017;**31**:245-253

[14] Gostariani R, Bagherpour E, Rifai M, Ebrahimi R, Miyamoto H. Fabrication of Al/AlN in-situ nanocomposite through planetary ball milling and hot extrusion of Al/BN: Microstructural evaluation and mechanical behavior. Journal of Alloys and Compounds. 2018;**768**:329-339

[15] Gostariani R, Asadi Asadabad M, Paydar MH, Ebrahimi R. Morphological and phase evaluation of Al/15wt.% BN nanocomposite synthesized by planetary ball mill and sintering. Advanced Powder Technology. 2017;**28**:2232-2238

[16] Lonardelli I, Zadra M, Ischia G, Barreiro JG, Bortolotti M, Molinari A. In situ synchrotron X-ray diffraction experiments on Ale15%BN mechanically alloyed powder: Observation of AlN nanoparticles precipitation and enhanced thermal stability of nanostructured Al matrix. Journal of Alloys and Compounds. 2009;**486**:653-659. DOI: 10.1016/j.jallcom.2009.07.024

[17] Gostariani R, Ebrahimi R, Asadi Asadabad M. The study of hot deformation behavior of mechanically milled and hot extruded Al-BN nanocomposite. Transactions of the Indian Institute of Metals. 2018;**71**:1127-1136. DOI: 10.1007/s12666-017-1248-x

[18] Suryanarayana C. Mechanical alloying and milling. Progress in Materials Science. 2001;**46**:1-184. DOI: 10.1016/S0079-6425(99)00010-9

[19] Soboyejo W. Mechanical Properties of Engineered Materials. New York: Marcel Dekker; 2002

[20] Zlateva G, Martinova Z. Microstructure of Metals and Alloys: An Atlas of Transmission Electron Microscopy Images. Boca Raton: CRC Press; 2008

[21] Lin Y, Xu B, Feng Y, Lavernia EJ. Stress-induced grain growth during hightemperature deformation of nanostructured Al containing nanoscale oxide particles. Journal of Alloys and Compounds. 2014;**596**:79-85. DOI: 10.1016/j.jallcom.2014.01.189

[22] Humphreys FJ, Hatherly M. Recrystallization and Related Annealing Phenomena. Oxford: Elsevier; 2004

[23] Singh D, Yun Y, Wan W, Grushko B, Zou X, Hovmöller S. A complex pseudo-decagonal quasicrystal approximant, Al37(Co, Ni)15.5, solved by rotation electron diffraction. Journal of Applied Crystallography. 2014;**47**:215. DOI: 10.1107/S1600576713029294

[24] Singh D, Yun Y, Wan W, Grushko B, Zou X, Hovmöller S. Hovmöller, structure determination of a pseudo-decagonal quasicrystal approximant by the strong reflections approach and rotation electron diffraction. Journal of Applied Crystallography. 2016;**49**:433. DOI: 10.1107/S1600576716000042

[25] Singh D, Shahi RR, Yadav TP, Mandal RK, Tiwari RS, Srivastava ON. Hydrogenation of (Zr69. 5Al7.5Cu12Ni11) 100-xTix quasicrystalline alloys and its effect on their structural and microhardness behavior. Journal of Non-Crystalline Solids. 2013;**380**:11-16. DOI: 10.1016/j.jnoncrysol.2013.08.024

[26] Singh D, Yadav TP, Tiwari RS, Srivastava ON, Singh M, Mandal RK. Nanoindentation studies of metallic glasses and nanoquasicrystal–glass composites in Zr–Al (Ga)–Cu–Ni alloys. International Journal of Nanoscience. 2011;**10**:929-933. DOI: 10.1142/S0219581X11008769